Mitochondria modulate programmed neuritic retraction

Sergei V. Baranov[a], Oxana V. Baranova[a], Svitlana Yablonska[a], Yalikun Suofu[a], Alberto L. Vazquez[b,c], Takashi D. Y. Kozai[c], X. Tracy Cui[c], Lisa M. Ferrando[a], Timothy M. Larkin[a], Yulia Y. Tyurina[d], Valerian E. Kagan[d,e,f], Diane L. Carlisle[a], Bruce S. Kristal[g], and Robert M. Friedlander[a,1]

[a]Neuroapoptosis Laboratory, Department of Neurological Surgery, University of Pittsburgh School of Medicine, Pittsburgh, PA 15213; [b]Neuroimaging Laboratory, Department of Radiology, University of Pittsburgh, Pittsburgh, PA 15219; [c]Department of Bioengineering, University of Pittsburgh, Pittsburgh, PA 15260; [d]Department of Environmental and Occupational Health, University of Pittsburgh, Pittsburgh, PA 15213; [e]Center for Free Radical and Antioxidant Health, University of Pittsburgh, Pittsburgh, PA 15213; [f]Laboratory of Navigational Redox Lipidomics, I.M. Sechenov First Moscow State Medical University, Moscow, Russia 119991; and [g]Division of Sleep and Circadian Disorders, Department of Medicine, Brigham and Women's Hospital, Harvard Medical School, Boston, MA 02115

Neuritic retraction in the absence of overt neuronal death is a shared feature of normal aging and neurodegenerative disorders, but the intracellular mechanisms modulating this process are not understood. We propose that cumulative distal mitochondrial protein damage results in impaired protein import, leading to mitochondrial dysfunction and focal activation of the canonical apoptosis pathway in neurites. This is a controlled process that may not lead to neuronal death and, thus, we term this phenomenon "neuritosis." Consistent with our hypothesis, we show that in primary cerebrocortical neurons, mitochondrial distance from the soma correlates with increased mitochondrial protein damage, PINK1 accumulation, reactive oxygen species production, and decreased mitochondrial membrane potential and depolarization threshold. Furthermore, we demonstrate that the distance-dependent mitochondrial membrane potential gradient exists in vivo in mice. We demonstrate that impaired distal mitochondria have a lower threshold for focal/nonlethal neuritic caspase-3 activation in normal neurons that is exacerbated in aging, stress, and neurodegenerative conditions, thus delineating a fundamental mechanistic underpinning for synaptic vulnerability.

neurodegeneration | mitochondrial membrane potential | neurite retraction | caspase-3 | mutant huntingtin

Neuritic retraction broadly describes synaptic pruning as well as axonal or dendritic regression. Physiologic neuritic retraction is a normal characteristic of brain development (1). Interestingly, neuritic retraction appears to involve intracellular focal caspase activation (2, 3) and extracellular complement and microglial activation (4) that do not lead to immediate neuronal death. The propagation of focally activated caspase-3 is delayed by the X-linked inhibitor of apoptosis protein (XIAP), a caspase inhibitor, which itself is cleaved by caspase-3 and -7 (3, 5). Pathologic neuritic retraction followed by neuronal death is a hallmark of neurodegenerative disorders. Stress-induced focal caspase activation leads to synaptic dysfunction and, once a threshold is reached, results in neuronal death, as it occurs in neurodegenerative diseases (6–8). However, although the relationship between caspase activation and mitochondrial dysfunction is established in cell death, the intracellular mechanisms that lead to focal caspase activation in physiologic and pathologic neuritic retraction are not understood.

Mitochondrial dysfunction occurs early in neurodegeneration. In Huntington's disease, mutant huntingtin (mHTT) directly binds to the mitochondrial protein import complex TIM23, disrupting mitochondrial protein import (9). Synaptic mitochondria are more vulnerable than nonsynaptic mitochondria to mHTT-induced inhibition of mitochondrial protein import, and blocking mitochondrial protein import induces caspase-3–dependent neuronal cell death (9). Given the global neuronal expression of mHTT, the

underlying mechanism that causes synaptic mitochondria to be more sensitive to mHTT-dependent protein import disruption is not clear. Furthermore, the relationship between synaptic mitochondrial protein import and focal caspase-3 activation is not known.

In this report, we investigate the mitochondrial mechanisms that initiate focal caspase activation in physiologic neuritic retraction. We demonstrate that progressive distal mitochondrial protein damage resulting in impaired mitochondrial protein import in distal neuronal compartments leads to neuritic retraction-related focal caspase-3 activation. This import defect further amplifies mitochondrial vulnerability by slowing incorporation of newly produced proteins, affecting mitochondrial physiology as indicated by loss of membrane potential, increased reactive oxygen species (ROS) production, and focal caspase-3 activation. We describe this fundamental physiologic mechanism that controls neurite plasticity/vulnerability and is amplified during stress and neurodegeneration as "neuritosis." This neuronal regulatory mechanism is likely important for neurodevelopment and is path-

Significance

Neuritic retraction in the absence of overt neuronal death occurs during aging and early in neurodegenerative disorders. However, mechanisms responsible for physiologic and pathologic neuritic retraction are unknown. We demonstrate that progressive distal mitochondrial protein damage, resulting in impaired mitochondrial protein import in distal neuronal compartments, leads to the neurite loss-related focal caspase-3 activation. This import defect amplifies mitochondrial vulnerability by slowing incorporation of newly produced proteins, affecting mitochondrial physiology indicated by loss of membrane potential, increased reactive oxygen species production, and focal caspase-3 activation. We describe this fundamental physiologic mechanism that controls neurite plasticity/vulnerability and is further amplified during neurodegeneration as "neuritosis." This neuronal regulatory mechanism is likely important for neurodevelopment and is exacerbated during aging and pathologically in neurodegenerative diseases.

www.manaraa.com

ologically exacerbated during aging, stress, and neurodegenerative diseases.

Results

Elevated Neuritic Caspase-3 Activity Is Associated with Mitochondrial Damage.

Distal neuronal compartments, including synapses, are more vulnerable to stress than the soma (10–12). Therefore, we evaluated in adult mice whether baseline caspase-3 activity is higher in forebrain synaptosomes compared with whole-forebrain lysates. Synaptosomes contain the cytosol of distal neuronal processes. Caspase-3/-7 enzymatic activity was assessed in whole-forebrain and synaptosomal lysates, as we found the enzymatic assay to be more sensitive in detecting caspase activation in our tissue samples. Caspase activity was 2.2-fold higher in synaptosomal fractions than in forebrain homogenates (Fig. 1*A*), indicating elevated caspase activity in distal neuronal compartments. This difference may reflect the fact that the forebrain contains a variety of cells, both of neuronal and nonneuronal (glial) origin, while synaptosomes are of neuronal origin (13). This initial in vivo demonstration establishes the relevance of the mechanisms in mature, live animals, leading to focus on neurons over other cell types found in the forebrain.

We therefore evaluated whether caspase-3 is activated in aged primary cerebrocortical neurons (PCNs). We found that, although PCNs aged for 14 d appeared morphologically healthy, there was more active caspase-3 after 14 d in vitro (DIV14) compared with 5 d in vitro. The activation of caspase-3 was correlated with a decreased level of the inhibitor of caspase-3, XIAP (Fig. 1*B*). To localize caspase-3 activity in neurons, we used a genetically encoded FRET biosensor. Caspase-3 is focally activated in neurites of healthy-appearing DIV14 PCNs, while no active caspase-3 is detected in the soma of the same PCNs. Focal caspase-3 activity was lower in younger PCNs (DIV8). Incubation of DIV14 PCNs with the broad caspase inhibitor zVAD-fmk abolished caspase-3 signal (Fig. 1*C*), confirming assay specificity. Incubating DIV14 PCNs with 10 μM glutamate (an in vitro model of the excitotoxicity) sequentially induced distal caspase-3 activation followed by loss of neurite integrity and, finally, activation of somal caspase-3 (*SI Appendix*, Fig. S1*A*). These data suggest a lower threshold for glutamate-induced caspase-3 activation in neurites compared with the soma. We demonstrate that glutamate-induced caspase-3 activation is associated with cleavage of XIAP (itself a caspase-3 substrate) and synaptic loss (as evidenced by PSD-95 reduction) in PCNs in a dose-dependent manner (*SI Appendix*, Fig. S1*B*). We also found that pure neurites (*SI Appendix*, Fig. S1*C*) of healthy PCNs have lower XIAP levels than whole cells (Fig. 1*D*). Thus, our data indicate that focal neurite caspase-3 activation was associated with loss of XIAP in neurites, likely due to caspase-3 activation, and that in healthy PCNs, low-magnitude distal caspase activation is not associated with cell death. The presence of a stressor such as glutamate, however, increases the magnitude of caspase-3 activation, leading to additional XIAP cleavage and subsequent synaptic loss as determined by loss of PSD-95.

Caspase-3 is activated following cytochrome *c* (cyt c) release from mitochondria (14). Reduction of mitochondrial membrane potential ($\Delta\psi_m$) results in cyt c release. We evaluated markers of $\Delta\psi_m$ in somal and distal neuronal compartments. PINK1 accumulates in depolarized mitochondria, and we found that it is increased in mitochondria isolated from DIV10 PCN neurites (Fig. 1*E*) compared with mitochondria isolated from whole-PCN lysates. PINK1 accumulation in mitochondria requires parkin recruitment to initiate mitophagy. Interestingly, parkin content is not increased in neuritic mitochondria, suggesting that mitophagy is not initiated, despite mitochondrial PINK1 accumulation. Damaged mitochondria not removed by mitophagy can release cyt c, triggering caspase-3 activation. Thus, we evaluated the soma and neurites for mitochondrial cyt c content using microfluidic chambers with 150-μm

tunnels that separate neurites from the soma. After growing PCNs in the chambers, we quantified colocalization of cyt c with translocase of the mitochondrial outer membrane 20 (TOM20) in the soma and neurites (Fig. 1 *F* and *G*). Release of cyt c (either because of the rupture of the inner membrane or Bax-mediated outer-membrane pore formation) may lead to a decrease of the ratio between soluble cyt c and membrane-bound TOM20, indicating leakage of the proapoptotic factor from mitochondria. Neurites have a lower cyt c/TOM20 ratio (Fig. 1*H*) and less colocalization of cyt c and TOM20 than the soma (Fig. 1*I*). We note that *R*-squared of the linear regression of the data shown in Fig. 1*H* is 0.11, suggesting that the cyt c/TOM20 ratio cannot be described solely by a linear model. Regardless of the low *R*-squared, difference between ratios in the soma versus distal neurites (Fig. 1*I*) remains significant. Furthermore, neurite cytosolic extracts demonstrate greater amounts of released cyt c than detected in somal extracts. Complementing the above finding, mitochondria isolated from neurites contained less cyt c, correlating with focal neurite caspase-3 activation (Fig. 1*J*).

Neuritic Mitochondrial Proteins Are Damaged and Replacement with de Novo Synthesized Proteins Is Delayed.

Optimal mitochondrial function is dependent upon a continuous cargo of functional proteins. As mitochondria age, they accumulate oxidized proteins, resulting in progressive mitochondrial dysfunction (15–18). To assess mitochondrial protein content quality, we used a mitochondria-targeted DsRED-E5 fluorescent protein (Mito-Timer) that changes fluorescence emission from green to red as it is oxidized (19). Thus, the red/green ratio was used to monitor the proportion of oxidized mitochondrial protein content (Fig. 2*A*). Single-cell analysis demonstrated that distal mitochondria have a greater red/green ratio, indicating an increased fraction of oxidized proteins in distal compared with proximal mitochondria (Fig. 2*B*). Incubation of neurons with the pan-caspase inhibitor zVAD-fmk did not affect distal mitochondrial protein oxidation (*SI Appendix*, Fig. S1*D*), indicating that this process is upstream of, or independent from, caspase activation. Our data suggest that, compared with somal mitochondria, distal mitochondria have slower protein turnover and/or greater ROS production, leading to an increase of oxidized mitochondrial protein cargo.

A characteristic of dysfunctional mitochondria is increased ROS production (20, 21). To assess spatial distribution of mitochondrial ROS in PCNs, we used MitoSOX, a probe that increases its fluorescence when it reacts with $O_2^{\bullet-}$. MitoSOX has a positively charged group that drives it into live mitochondria in accordance with $\Delta\psi_m$. Therefore, fluorescence intensity of MitoSOX in mitochondria depends on both $O_2^{\bullet-}$ and $\Delta\psi_m$. To control for $\Delta\psi_m$-dependent MitoSOX accumulation, we used MitoView633, another $\Delta\psi_m$-dependent mitochondrial dye that fluoresces independent of $O_2^{\bullet-}$ levels. To identify all mitochondria, we transfected PCNs with a green fluorescent protein (GFP) fused with a mitochondrial targeting sequence (mtGFP) (Fig. 2*C*). Since both dyes are single-charged species and their spectral properties are well-separated at the equilibrium state, a ratio of MitoSOX/MitoView633 characterized $\Delta\psi_m$-independent mitochondrial $O_2^{\bullet-}$ distribution across the neuron. We found that distal mitochondria have higher ROS production levels than their somal counterparts (Fig. 2*D*). These data are concordant with increased oxidized protein content in distal mitochondria.

Replacement of oxidized mitochondrial proteins is determined by the efficiency of de novo protein synthesis followed by import into mitochondria. To determine the mechanism for accumulation of oxidized protein in distal mitochondria, we evaluated the kinetics of mitochondrial protein accumulation and distribution. Following mtGFP transfection, we first detected green mitochondria in the soma (Fig. 2*E*). It is likely that the initial, and bulk of, protein translation occurs in the perinuclear area and, therefore, somal mitochondria are the first to import mtGFP. Distal

www.manaraa.com

NEUROSCIENCE

mitochondria also received newly translated proteins, as judged by the ratio of mtGFP intensity in proximal versus distal mitochondria at different times following transfection. Progressively follow-ing transfection for 12 d, the ratio of distal-to-proximal mtGFP approaches one (Fig. 2F). Given that 95% of protein synthesis occurs in neuronal soma (22), our data suggest that mtGFP is
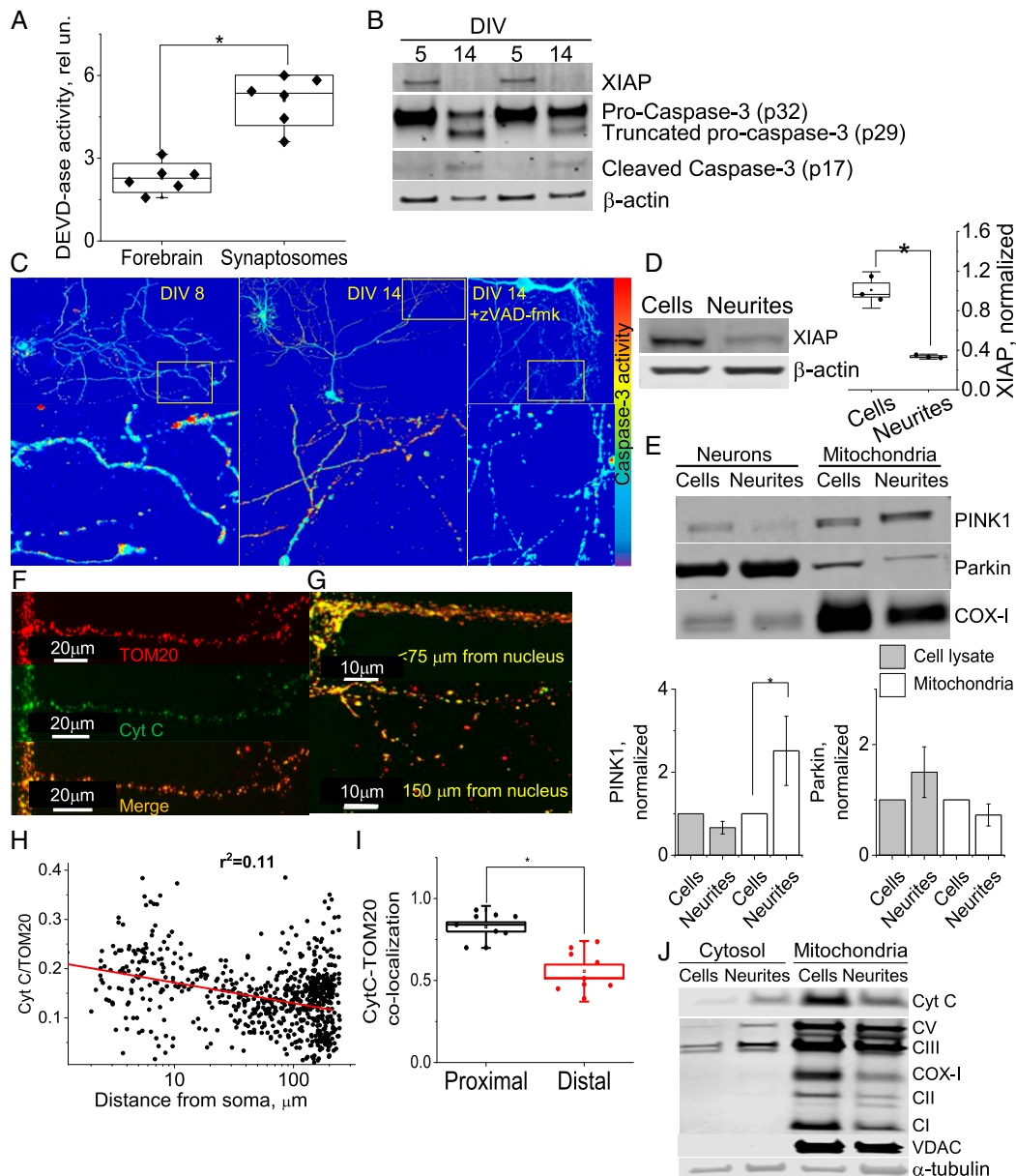

Fig. 1. Elevation of focal axodendritic caspase-3 activity is associated with decreased neuritic mitochondrial cyt c content. (*A*) Synaptosomes isolated from mouse brains are characterized by elevated caspase-like (DEVD-ase) activity (*$P < 0.001$, two-tailed t test) compared with whole-forebrain lysates. Data are shown as a box chart; $n = 6$. (*B*) Immunoblotting shows a reduction of apoptosis-inhibiting protein (XIAP), reduction in pro-caspase-3 (p32), increase of the cleaved caspase-3 precursor (p29), and appearance of cleaved caspase-3 in PCNs upon aging in culture. Each lane represents one culture; this is representative of three wells. (*C*) Elevated DEVD-ase activity in neurites is more robust in mature (DIV14) compared with young (DIV8) PCNs and is decreased in the presence of a pan-caspase inhibitor (zVAD-fmk; 5 μM). Each condition was repeated five times and the images are representative. Boxed regions are enlarged in the corresponding images of the bottom row. (*D*) Immunoblotting quantification shows a neurite-specific decrease of XIAP in PCNs of DIV10. Each lane represents cells or neurites collected from one well of a multiwell cell-culture plate as described in *Methods*; representative image of $n = 3$ (*$P = 0.012$, paired t test). (*E*) Representative immunoblot and quantitation for PINK1 and parkin in PCNs, neurites, and isolated mitochondria. Immunoblotting shows that isolated neuritic mitochondria accumulate more full-length PINK1 and less parkin compared with PCN mito-chondria (DIV10). Mitochondrial cyt c oxidase (respiratory complex IV) subunit 1 (COX-I) was used as a loading control (*$P = 0.03$, t test; $n = 3$; data are shown as mean +/− SD). (*F*) Immunostaining of PCNs cultured in a microfluidic chamber to compartmentalize neurites and the soma. PCNs (DIV14) were fixed and stained against TOM20 and cyt c. (*G*) Close-up of the soma and axon up to 75 μm (*Top*) and >150 μm (*Bottom*) from the nuclear compartments demonstrates reduced cyt c signal. Red mitochondria have reduced cyt c (green) content. (*H*) Analysis of TOM20 and cyt c signal shows a distance-dependent decrease of the ratio of colocalized red (TOM20) and green (cyt c) signals. Each dot represents one mitochondrial volume (total 716 mitochondrial volumes per neuron). (*I*) Decreased colocalization [presented as Pearson's colocalization coefficient (51)] of TOM20 and cyt c in distal (>150 μm from nucleus) compared with perinuclear mitochondrial volumes (*$P < 0.0001$, paired t test; $n = 9$ neurons, total 4,894 mitochondrial volumes; data are shown as mean +/− SD). (*J*) Content of mitochondrial proteins CI (subunit NDUFB8), CII (subunit SDHB), CIII (core protein 2), COX-I, CV (alpha subunit), and VDAC (voltage-dependent anion-selective channel protein 1, a porin of the outer mitochondrial membrane) of the cytosolic fraction of PCNs and of neurites (2 μg total protein) (DIV14) as well as mitochondria isolated from PCNs and neurites (10 μg total protein). Tubulin was used as loading control for cytosolic fractions and an impurity indicator for isolated mitochondria; representative image of $n = 3$.
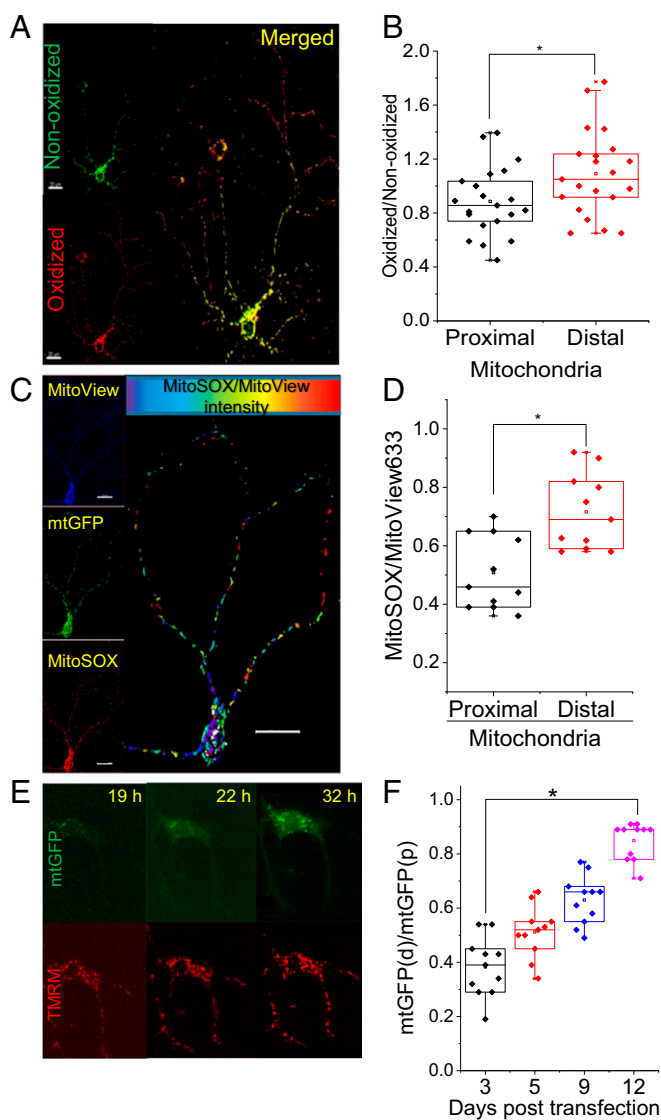
www.manaraa.com

Fig. 2. Distal neuritic mitochondria have higher levels of oxidized proteins, increased ROS production, and slower protein import compared with perinuclear mitochondria. (*A*) Representative dual-channel image of a DIV5 neuron using a 40×, N.A. 0.95 objective taken 24 h after transfection with MitoTimer and shown as a maximum-intensity profile for a series of z stacks. (Scale bars, 20 μm.) (*B*) Quantification of the protein content quality of proximal (≤10 μm from nucleus) and distal (≥70 μm from nucleus) mitochondria (*$P < 0.0001$, paired-sample t test; $n = 21$ neurons, total 3,590 mitochondrial volumes). (*C*) DIV7 neurons were imaged 24 h after transfection with mtGFP (green) and 1 h after addition of MitoSOX (violet) and MitoView633 (red) dyes. The MitoSOX/MitoView633 ratio represents $\Delta\psi_m$-independent MitoSOX fluorescence intensity (shown as a heatmap in which blue is low and red is high) affected by mitochondrial $O_2^{\bullet-}$. (Scale bars, 20 μm.) (*D*) Quantification of the MitoSOX/MitoView633 ratio of proximal (≤10 μm from nucleus) and distal (≥70 μm from nucleus) mitochondria (*$P = 0.001$, paired t test; $n = 11$ PCNs, total 2,750 mitochondrial volumes). (*E*) Induction of mitochondrial protein import occurs earliest in the perinuclear area. DIV5 PCNs transfected with mtGFP were imaged over the indicated time period. Representative image from three independent experiments. (Scale bar, 10 μm.) (*F*) Time-dependent changes in the mtGFP signal intensities of distal (≥50 μm from nucleus) mitochondria (d) in comparison with perinuclear (≤10 μm from nucleus) mitochondria (p). All images (z stacks) were collected with a confocal fluorescence microscope using a 40×, N.A. 0.95 objective. Data are shown for 5 neurons imaged 3 d posttransfection and 12 neurons imaged 6, 9, and 12 d posttransfection. The asterisk indicates statistically significant differences between the mitochondrial populations on days 3 and 12 posttransfection (*$P < 0.001$, Mann–Whitney U test). All data are shown as mean +/− SD.

first imported into somal mitochondria while new protein for import is available to distal mitochondria after a delay. Thus, protein content renewal in somal mitochondria is limited by mitochondrial protein import, while renewal in distal mitochondria is limited by the transport of somal mitochondria to neuronal terminals and the subsequent exchanging of their protein content via the fusion/fission process with distal mitochondria. Proteins may also be transported or translated distally (23, 24) and then imported into stationary mitochondria.

Distance-Dependent $\Delta\psi_m$ Decline in Neuronal Mitochondria in Vitro and in Vivo. Given the differences in protein import and oxidized protein content between somal and distal mitochondria and the increased neurite vulnerability to stress, we evaluated whether there was a neuronal compartment-specific difference in baseline $\Delta\psi_m$. To address this question, we applied a two-parameter live-cell imaging approach to measure $\Delta\psi_m$ changes in a neuronal population of mitochondria based on simultaneous permanent (mtGFP) and dynamic tetramethylrhodamine methyl ester (TMRM) mitochondrial labeling. This approach is optimal for live-cell imaging because it involves a genetically encoded mitochondrial indicator that, in contrast to MitoTracker (25), introduces minimal interference to mitochondrial physiology (26). TMRM allows dynamic $\Delta\psi_m$ imaging over time since, in nonquenching mode, TMRM has low toxicity. Thus, mtGFP provides mitochondrial volume information and TMRM indicates $\Delta\psi_m$ changes. We imaged DIV5 and DIV14 PCNs using confocal fluorescence microscopy to obtain a series of z stacks used to determine mitochondrial volumes. TMRM intensity, calculated as mean voxel intensity over mtGFP-defined voxels, reflects $\Delta\psi_m$ for the assessed mitochondrial population. Because of optical limitations, we cannot resolve mitochondrial pairs near each other; therefore, the mean value for TMRM fluorescence intensity is assigned to mitochondrial volume rather than a single mitochondrion (Fig. 3*A*). Accumulation of TMRM in mitochondria (assessed as fluorescence signal intensity increase) is proportional to $\Delta\psi_m$ (27), decreased with distance from the nucleus, and we approximated it with an apparent linear fit upon presenting a distance (x scale) as a logarithmic scale, whereby $\Delta\psi_m$ decline is expressed as the slope of the line. We demonstrate that in both DIV5 and DIV14 PCNs there is a progressive distance-dependent degradation of $\Delta\psi_m$ with somal mitochondria having higher membrane potential than distal mitochondria. Furthermore, DIV14 PCNs had a steeper slope than DIV5 PCNs (Fig. 3*B*), suggesting a time-dependent decrease in $\Delta\psi_m$ in distal mitochondria. We note that, over time, the difference in mtGFP between distal and somal mitochondrial populations decreased (compare mtGFP distance-dependent slope in DIV5 and DIV14 neurons in Fig. 3*B*), indicating delayed protein import in distal mitochondria.

Mitochondria are transported anterogradely and retrogradely along neurites. Given the $\Delta\psi_m$ gradient (Fig. 3*A*), we evaluated the $\Delta\psi_m$ of anterograde versus retrograde mitochondria. We found greater $\Delta\psi_m$ in anterograde compared with retrograde mitochondria (Fig. 3*C* and Movie S1). Thus, our observation is consistent with the reported positive correlation between anterograde mitochondria and high $\Delta\psi_m$ (28). Anterograde mitochondria also had a lower oxidized protein ratio, as measured with MitoTimer, than retrograde mitochondria (Fig. 3*D*), suggesting that anterograde mitochondria deliver newly synthesized proteins to distal stationary mitochondria and retrograde mitochondria transport damaged proteins back to the soma. We did not find any motile mitochondria that were fully depolarized (i.e., mitochondrial TMRM fluorescence equal to background fluorescence), suggesting that $\Delta\psi_m$ is required for mitochondrial motility. Because the motile mitochondria fraction is small (26), the observed distance-dependent $\Delta\psi_m$ gradient can be assigned to the stationary neuronal mitochondrial population.

Given the in vitro demonstration of a distance-dependent $\Delta\psi_m$ gradient, we determined whether a similar finding occurs in vivo.
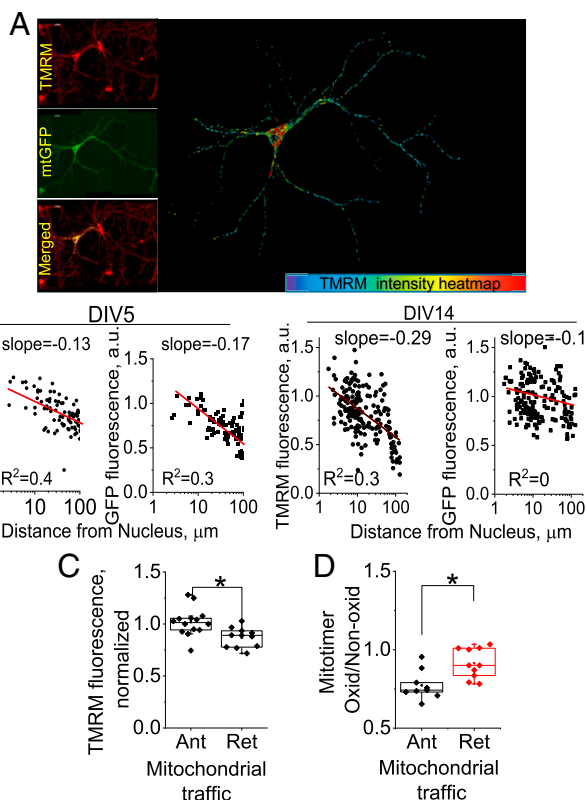
Baranov et al.

www.manaraa.com

Fig. 3. $\Delta\psi_m$ is negatively correlated with distance from the nucleus. (*A*) Representative image of a PCN transfected with mtGFP and loaded with 50 nM TMRM. (*A*, *Left*) TMRM signal, GFP signal, and merged. (*A*, *Right*) TMRM fluorescence intensity heatmap demonstrating a gradual proximal-to-distal gradient of loss of $\Delta\psi_m$. (Scale bars, 20 μm.) (*B*) Representative analysis of the TMRM and mtGFP fluorescence intensities' dependence on the distance between mitochondria and nuclei for DIV5 neurons (*Left*) and DIV14 neurons (*Right*) transfected 2 and 9 d before imaging. TMRM and GFP fluorescence are presented as mean values of the voxel intensities for a given mitochondrial volume defined via mtGFP signal after 3D reconstruction of z-stack images collected using a 40×, N.A. 0.95 objective. Symbols represent individual mitochondrial volumes. Apparent linear regression with the slope indicated is shown as a line plot. (*C*) Comparison of TMRM fluorescence of anterograde and retrograde mitochondria normalized by TMRM signal intensity of stationary mitochondria. Data are for 25 mitochondria (14 anterograde and 11 retrograde) observed in 12 neurons in five independent experiments (*$P = 0.015$, Wilcoxon signed-rank test; data are shown as mean +/− SD). (*D*) Comparison of the MitoTimer fluorescence of anterograde and retrograde mitochondria (9 anterograde and 10 retrograde observed in six neurons in three independent experiments) (*$P = 0.006$, Mann–Whitney U test; data are shown as mean +/− SD). Ant, anterograde; Ret, retrograde.

Dorsal spinal cord white-matter tracts (dorsal columns) provide an anatomical substrate to evaluate superficial parallel unidirectional well-organized sensory tracts (fasciculus gracillis and fasciculus cuneatus). The proximal axon is caudal and the distal axon is rostral. We studied the spinal cord of live mice using two-photon microscopy to detect TMRM fluorescence from the surface to a depth of 100 to 200 μm. To specifically image neuronal mitochondria, we used Thy1-Mito-CFP transgenic mice, where all neuronal mitochondria have cyan fluorescent protein (CFP). The thecal sac was surgically exposed and the dura matter was removed to increase TMRM penetration into the spinal cord. One hour later the dye was carefully washed out, and images from CFP and TMRM channels were recorded and analyzed as described. A representative raw image from one experiment and analysis is shown in Fig. 4*A* and *SI Appendix*, Fig. S2*A*. A total of eight adult mice were imaged and all demonstrated equivalent

results (*SI Appendix*, Fig. S2*B*). We note that distribution of the TMRM between mitochondria and the cytoplasm is affected by a difference in the thickness of the neuronal cells (i.e., cell body and axons) that comprise spinal cord neuronal tracts. Therefore, we did not image neuronal bodies, to minimize sample thickness effect. Use of the two-photon microscopic technique also reduced possible errors associated with insufficient excitation of the thick tissue. The analysis demonstrates that the intensity of TMRM signal of neuronal mitochondria decreases with distance from neuronal bodies, while CFP signal intensity remains constant (Fig. 4*B*). These data confirm the existence of the neuronal distance-dependent $\Delta\psi_m$ gradient in vivo.

Mitochondrial Protein Import Disruption Causes Distal $\Delta\psi_m$ Decrease and Caspase-3 Activation. Neurodegenerative conditions are often associated with disturbance of mitochondrial function, including mitochondrial trafficking and protein import (9, 29). To induce mitochondria-specific stress, we used an shRNA to knock down a translocase of the outer mitochondrial membrane (TOM40), a key protein in the import of matrix and intermembrane mitochondrial proteins. Efficacy of TOM40 knockdown using this construct is shown in *SI Appendix*, Fig. S4*E*, and inhibition of mitochondrial protein import was previously demonstrated (9). We detected sequential $\Delta\psi_m$ loss followed by cellular fragmentation culminating in PCN death (blue nuclear staining; Fig. 5 *A* and *B* and Movie S2). Both $\Delta\psi_m$ loss and cellular
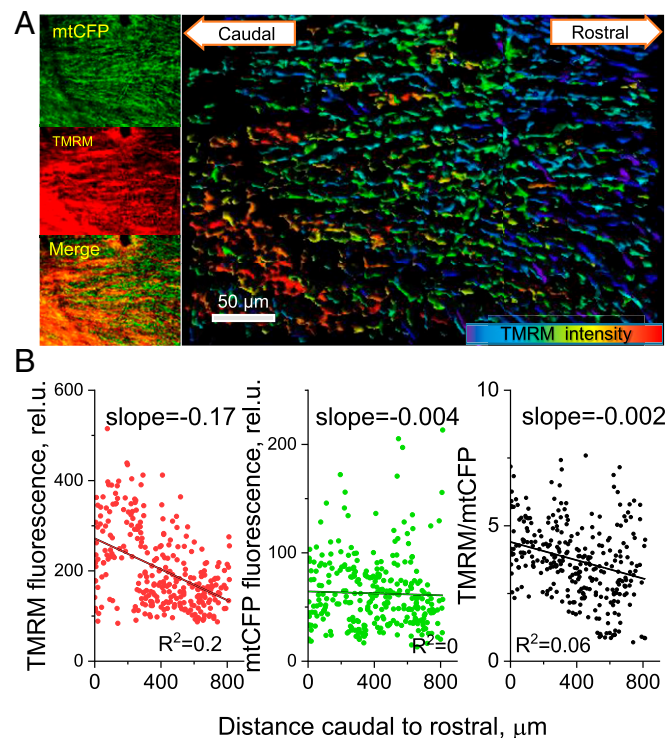

Fig. 4. In vivo dual-channel two-photon images of mouse spinal cord neuronal mitochondria. (*A*) Representative images of a Thy1-CFP mouse spinal cord exposed to TMRM. (*A*, *Left*) TMRM signal, CFP signal, and merged images. (*A*, *Right*) TMRM fluorescence intensity heatmap demonstrating a gradual proximal-to-distal gradient of $\Delta\psi_m$. (*B*) Representative analysis of the TMRM and mtCFP fluorescence intensity, and their ratio along the imaged spinal cord. TMRM and CFP fluorescence intensities are presented as mean values of the pixel intensities for a given mitochondrial volume defined as mtCFP signal after 3D reconstruction of z-stack images collected using a 20×, N.A. 1 objective. Each dot represents a mitochondrial volume. Plotted linear regression line of best fit shows the slope of the TMRM signal (normalized to mtCFP) to be significantly different from zero ($R^2 = 0.06$, $P = 5 \times 10^{-6}$).
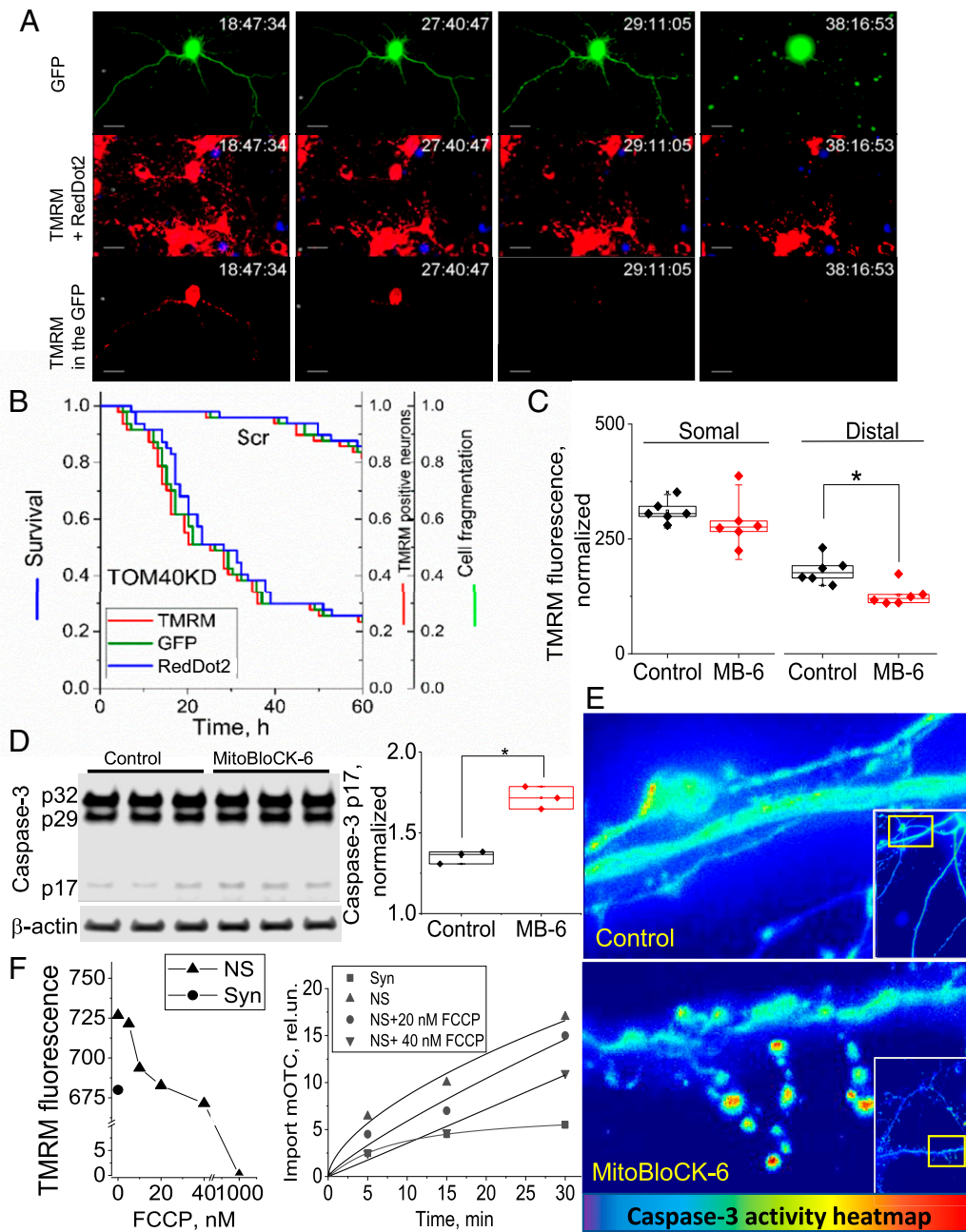
www.manaraa.com

Fig. 5. Disruption of mitochondrial import causes early mitochondrial depolarization of distal mitochondria followed by caspase-associated neuronal cell death. (*A*) TOM40 knockdown (TOM40KD) induced mitochondrial depolarization followed by segmentation in a distal-to-proximal direction. Live-cell imaging of TOM40KD neurons in the presence of TMRM and cell-impermeable RedDot2 nuclear (stains nucleus blue in dead cells) dyes. DIV5 cortical neurons were transfected with a U6-TOM40/CMV-GFP plasmid. At DIV8, loss of mitochondrial membrane potential and cell death were assessed using TMRM and RedDot2 using live confocal imaging. Time 0 indicates the beginning of imaging, and timestamps on images are h:min:s. To better appreciate the temporal and site-specific pattern of $\Delta\psi_m$ loss,, *Bottom* panels demonstrate TMRM staining only of the green transfected neuron. (Scale bars in all panels, 20 μm.) (*B*) Survival plot of neurons transfected with U6-TOM40/CMV-GFP (TOM40KD) ($n = 49$ neurons, three independent experiments) and U6-Scr/CMV-GFP (Scr, scrambled) ($n = 47$ neurons, three independent experiments). Equality of survival functions tested with log rank is shown in the graph. (*C*) Prolonged (72-h) incubation of PCNs with 2 μM MitoBloCK-6 (MB-6; $\Delta\psi_m$-independent mitochondrial protein import blocker) resulted in lowering of the $\Delta\psi_m$ of distal (>50 μm from nucleus) (*$P = 0.005$, t test) compared with somal (≤10 μm from nucleus) mitochondria. (*D*) Prolonged (72-h) incubation of PCNs with MitoBloCK-6 induced caspase-3 activation (*$P = 0.027$, paired-sample t test). Data are shown as a box chart; $n = 3$. (*E*) Neuritic caspase-3 activation in PCNs (DIV21) after 72 h of incubation with 2 μM MitoBloCK-6 visualized as CFP/FRET signal ratio in neurons transfected with genetically encoded caspase-3 FRET substrate. Image color ranged from blue to red, representing minimum and maximum DEVD-ase activity, respectively. A representative image of five pyramidal cortical neurons obtained from four independent experiments is shown. (*F*) Lower protein import activity as measured by pOTC cleavage and generation of mOTC of synaptosomal (Syn) mitochondria compared with nonsynaptosomal (NS) mitochondria at equal $\Delta\psi_m$. Protein import activity was quantified in synaptosomal mitochondria and in isolated nonsynaptosomal mitochondria supplied with 20 to 40 nM carbonyl cyanide-p-trifluoromethoxyphenylhydrazone (FCCP).

fragmentation first occurred in neurites, suggesting a greater vulnerability of distal synaptic mitochondria compared with somal mitochondria.

To complement the above-described genetic approach of evaluating inhibition of mitochondrial protein import, we evaluated a pharmacologic import inhibitor. MitoBloCK-6, a specific

inhibitor of Erv1/ALR, interrupts import and assembly of mitochondrial intermembrane proteins without affecting $\Delta\psi_m$ (30). We tested the ability of the compound to affect basic bioenergetic properties of isolated neuronal mitochondria. We did not find any interference with mitochondrial respiration parameters (resting state, ADP-stimulated and FCCP-stimulated respiration) measured in isolated mouse brain mitochondria at a concentration of 10 μM MitoBloCK-6 (*SI Appendix*, Fig. S4F). While incubation of PCNs with 2 μM MitoBloCK-6 for 2 h did not affect $\Delta\psi_m$ of PCNs, incubation for 72 h significantly reduced $\Delta\psi_m$ in distal neuronal compartments by 41% compared with a nonsignificant 8% reduction in somal $\Delta\psi_m$ (Fig. 5C), again demonstrating the greater vulnerability of distal mitochondria. Similarly, 72-h incubation with MitoBloCK-6 increased distal caspase-3 activation (Fig. 5 D and E), suggesting that mitochondrial vulnerability correlates with caspase-3 activation in distal neuronal compartments.

Distal mitochondria maintain and regulate neurotransmission by sequestering and buffering Ca^{2+}, including Ca^{2+} release after stimulation (31–33). Mitochondrial Ca^{2+} buffering regulates signaling, metabolism, and cell survival (34). The mitochondrial capacity to take up and accumulate Ca^{2+} is $\Delta\psi_m$-dependent. Mitochondria with lower $\Delta\psi_m$ have lower Ca^{2+}-retention capacity and a lower threshold to undergo Ca^{2+}-induced permeability transition, depolarization, and release of cyt c triggering caspase-3 activation. Our data demonstrate that distal mitochondria have delayed protein import, lower $\Delta\psi_m$, and higher oxidized protein cargo than somal mitochondria. We hypothesized that this may result in increased localized vulnerability to excitotoxicity. To test this, we exposed PCNs to excitotoxic glutamate concentrations, since the mechanism of glutamate-induced excitotoxicity is related to glutamate-induced increase of cytosolic Ca^{2+} that is sequestered by polarized mitochondria. Addition of glutamate induced dose-dependent mitochondrial depolarization, with distal mitochondria depolarizing first (*SI Appendix*, Fig. S3).

Mitochondrial protein import and $\Delta\psi_m$ are mechanistically linked. To demonstrate if the distal mitochondria import defect results from the decreased $\Delta\psi_m$, we compared the import activity of isolated nonsynaptosomal and synaptosomal mitochondria at the same $\Delta\psi_m$. Given that synaptosomal mitochondria have lower $\Delta\psi_m$ than nonsynaptosomal mitochondria, we identified an FCCP (mitochondrial uncoupler) concentration that would equalize the $\Delta\psi_m$ between the two distinct mitochondrial populations. In the presence of 20 to 40 nM FCCP, the $\Delta\psi_m$ of nonsynaptosomal mitochondria was similar to synaptosomal mitochondria. Still, the import rate [as measured by import and cleavage of premature (p) ornithine transcarbamylase (OTC) and generation of mature (m) OTC] was higher in FCCP-treated nonsynaptosomal mitochondria. This suggests that the import machinery of synaptic mitochondria is impaired and the $\Delta\psi_m$ is an indicator for disturbed mitochondrial homeostasis and not a proximal cause of reduced protein import (Fig. 5F).

Distal Mitochondria Defects Lead to Synaptic Vulnerability in Neurodegeneration. R6/2 mice express mHTT exon 1 and have been used as a model of Huntington's disease (HD) (35). Caspase-dependent neuronal dysfunction in R6/2 mice manifests as a reduction of neurotransmitter receptors. This reduction was corrected by caspase inhibition, providing evidence that caspase activation results in neuronal dysfunction before, and distinct from, cell death (36). Focal, sublethal synaptic caspase activation suggested by our data above provides a potential mechanistic explanation for these findings. While wild-type huntingtin (WT HTT) binds and inhibits active caspase-3 (37), the reduced ability of mHTT to bind caspase-3 likely enhances caspase-3 activation. This is relevant to the human disease, where there is one copy of WT HTT and one copy of mHTT. Thus, we analyzed focal caspase activation, mitochondrial protein import, mitochondrial protein oxidation, and distance-dependent $\Delta\psi_m$ in PCNs from R6/
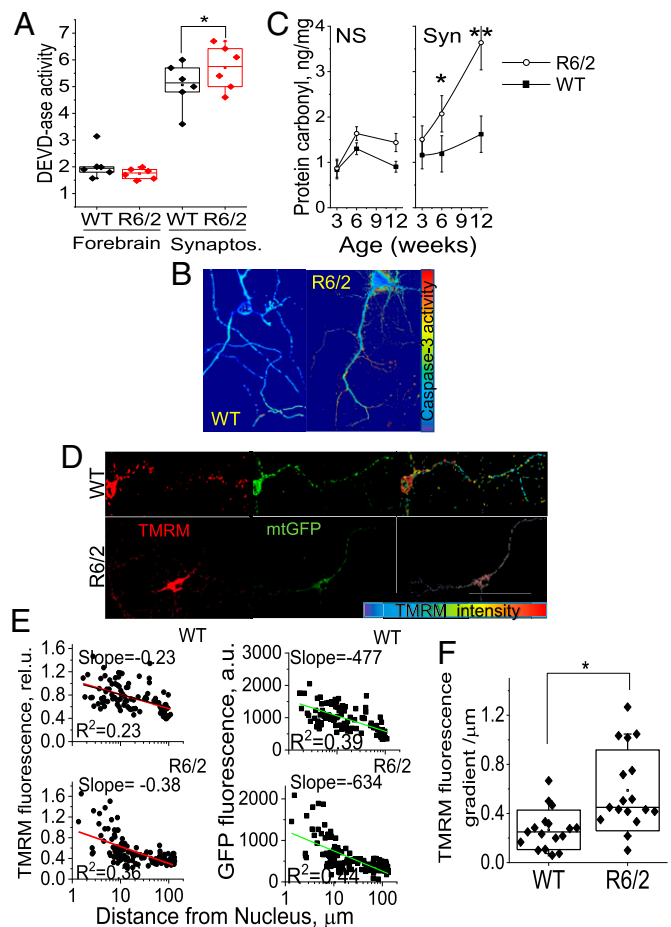

Fig. 6. mHTT expression is associated with elevated synaptosomal caspase-3 activity in R6/2 mice compared with WT, elevated caspase-3 activity in neurites, and lower $\Delta\psi_m$ in distal mitochondria. (A) Synaptosomes isolated from 6-wk-old (early symptomatic) R6/2 mouse forebrains have elevated DEVD-ase activity (*$P = 0.008$, t test) compared with WT samples, while DEVD-ase activity in WT and R6/2 forebrains is similar. Data are shown as a box chart; $n = 6$. (B) Elevated caspase-3 activity in neurites is more robust in R6/2 PCNs. The image is representative of 13 WT and 9 R6/2 PCNs obtained from three independent experiments. (C) Content of mitochondria of oxidized proteins is increased in R6/2 synaptosomal mitochondria associated with disease progression. Mitochondria were isolated from brains of R6/2 and WT mice at 3, 6, and 12 wk of age ($n = 3$ independent isolations of five brains per isolation). Mitochondrial protein quality was assessed by using a Protein Carbonyl Colorimetric Assay Kit (Cayman Chemical). The asterisk indicates statistically significant differences between the WT and R6/2 at 6 wk of age (*$P = 0.0014$, t test). The double asterisks indicate statistically significant differences between the WT and R6/2 at 12 wk of age (**$P = 0.007$, t test). (D) Distal mitochondria in R6/2 neurons have lower $\Delta\psi_m$. DIV5 PCNs from WT or R6/2 were transfected with mtGFP and loaded with 50 nM TMRM to probe $\Delta\psi_m$. Images were analyzed to obtain a mean value of TMRM fluorescence per mitochondrial volume defined by mtGFP signal. The image is representative of 17 WT and 17 R6/2 PCNs obtained from five independent experiments. (E) Representative analysis of the TMRM fluorescence intensity changes is presented as a gradient of the $\Delta\psi_m$ decrease with distance from the nucleus (slope). (F) Each symbol represents the TMRM fluorescence slope of transfected neurons; $n = 17$ obtained from five independent experiments. The asterisk indicates statistically significant differences between WT and R6/2 (*$P = 0.003$, t test).

2 mice. We found that caspase-3 activity was significantly greater in R6/2 synaptosomes than in WT (Fig. 6A). Focal caspase-3 activity was more robust in R6/2 compared with WT PCNs, as evidenced by more widespread neuritic caspase-3 activation (Fig. 6B). Similarly, using MitoTimer, we demonstrate a greater fraction of oxidized proteins in distal mitochondria of R6/2 PCNs than

Baranov et al.

www.manaraa.com

in WT (*SI Appendix*, Fig. S4*A*). These findings are consistent with our data discussed above and suggest that this site-specific damage is exacerbated by mHTT.

Given the greater proportion of oxidized proteins in distal mitochondria, particularly in R6/2 neurons, we directly evaluated mitochondrial damage in purified adult brain mitochondria from mice. We isolated functional brain mitochondria from 11- to 12-wk-old (symptomatic) R6/2 mice and determined that the yield of synaptosomal mitochondria was significantly lower than in WT, while the amount of nonsynaptosomal mitochondria was the same (*SI Appendix*, Fig. S4*B*). We further employed an independent assessment of synaptosomal and nonsynaptosomal mitochondria in WT and R6/2 mice using a specific mitochondrial phospholipid marker, cardiolipin (CL). Lower CL content (normalized to the total forebrain protein) was found in R6/2 compared with WT synaptosomal, but not nonsynaptosomal, mitochondria (*SI Appendix*, Fig. S4*C*). These combined results demonstrate a selective reduction of synaptic mitochondria in R6/2 brains. Furthermore, protein oxidative damage increased in synaptosomal (and not in nonsynaptosomal) mitochondria with disease progression in R6/2 brains, as indicated by an increase in protein carbonyl content (a marker of free radical damage) in isolated mitochondria (Fig. 6*C*). Finally, we evaluated whether the $\Delta\psi_m$ gradient is more pronounced in PCNs expressing mHTT. Analysis of the TMRM and mtGFP fluorescence of WT and R6/2 PCNs (Fig. 6 *D–F*) revealed that the $\Delta\psi_m$ gradient is steeper in R6/2 PCNs, and mtGFP content (assessed by GFP fluorescence intensity) also drops faster in R6/2 PCNs. The rate of mtGFP import in R6/2 neuronal mitochondria was slower compared with WT (*SI Appendix*, Fig. S4*D*), consistent with the mHTT-induced mitochondrial protein import defect that was previously reported in synaptosomal R6/2 mitochondria (9).

Interestingly, decreased $\Delta\psi_m$ is associated with the redistribution of CL from its normal localization in the inner mitochondrial membrane to the surface of the outer mitochondrial membrane, where it interacts with the autophageal protein LC3 and acts as an effective promitophageal signal (38). Using LC-MS–based assessments of CL externalization (38), we found significantly elevated levels of externalized CL on the surface of synaptosomal mitochondria compared with nonsynaptosomal mitochondria isolated from R2/6, and compared with WT mice (*SI Appendix*, Fig. S5). This suggests that decreased $\Delta\psi_m$ may be associated with higher demands for enhanced turnover of synaptosomal compared with nonsynaptosomal mitochondria.

Discussion

Protein oxidation is a normal event in the life cycle of a protein; however, we demonstrate that the ability to replace damaged proteins efficiently in neuritic mitochondria is compromised. Cumulative mitochondrial protein damage leads to impairment of mitochondrial function including protein import and a malfunctioning electron transport chain, resulting in further functional deterioration. We also found a distance-dependent decrease of the $\Delta\psi_m$, accumulation of full-length PINK1 in distal mitochondria without subsequent parkin recruitment, focal cyt c release, and caspase-3 activation in neurites of healthy neurons. The above-described cycle is not pathologic; it occurs under normal physiologic conditions. It has been shown that mitochondrial trafficking in neurons is significantly biased toward the anterograde direction (39), resulting in accumulation of mitochondria in distal neuronal compartments. With time, these mitochondria accumulate oxidized/damaged proteins and must be recycled (via mitophagy), most likely locally (40, 41). Here we show that retrograde-moving mitochondria have mitochondrial potential (although low). Therefore, we argue that when distal mitochondria become fully depolarized because of (oxidative) damage beyond repair, they undergo mitophagy. However, if they are still polarized, they may travel retrogradely for repair. Damaged distal mitochondria which are not eliminated via mitophagy may release mitochondria-harbored proapoptotic factors (i.e., cyt c), activating the caspase cascade. Thus, our data address key questions in the field regarding the upstream mechanisms that initiate focal caspase activation leading to physiologic neuritic retraction.

Pathologic neuritic retraction and synaptic loss are early events in neurodegeneration. Our findings, including exacerbation of the process described above due to excitotoxicity or mHTT expression, provide a mechanism for the selective neurite vulnerability to caspase-dependent pathologic neuritic retraction that is seen in neurodegenerative diseases such as HD (36).

In sum, we describe a process where focal mitochondria-mediated canonical caspase activation mediates physiologic neuritic retraction without cell death. We term this process neuritosis. Neuritosis is likely a normal, but previously unrecognized, mechanism responsible for developmental pruning, neuroplasticity, neuritic retraction during aging, and synaptic vulnerability. During neuritosis, accumulated damaged and malfunctioning mitochondria fail to recruit parkin to active mitophagy and instead release cyt c, focally activating the caspase cascade via apoptosome formation (42) in neurites. The accumulation of synaptic mitochondria with low $\Delta\psi_m$ is exacerbated in mHTT-expressing neurons, leading to pathologic neuritic retraction, providing an explanation of synaptic vulnerability in HD (9, 43). Understanding the consequences of neuronal mitochondrial heterogeneity and mitochondrial regulation of neuritosis may provide important information relevant to synaptic pruning demonstrated in normal development as well as aging and in neurodegenerative diseases. These data also suggest that synaptic mitochondria may be a target for the development of therapies for aging- and neurodegenerative disease-mediated synaptic loss.

Methods

Transgenic Mice. HD transgenic R6/2 mice carrying the promoter sequence and exon 1 of the human *mHTT* gene with ∼150 CAG repeats were obtained and maintained as previously described (9). Thy1-CFP-MitoS mice, which express mitochondria-targeted cyan fluorescent protein in neurons, were obtained from Jackson Laboratory. All live vertebrate experiments were performed in compliance with the NIH *Guide for the Care and Use of Laboratory Animals* (44). Animal protocols were approved by the University of Pittsburgh Institutional Animal Care and Use Committee.

Cell Culture, DNA Transfection, and Baculovirus Infection. R6/2 and littermate WT PCNs were prepared from embryonic day (E)15.5 embryos, as previously described (9). For live-cell imaging, neurons were cultured on poly-D-lysine–coated multiwall glass-bottom plates (Cellvis). For isolation of neuritic mitochondria, neurons were grown on poly-D-lysine–coated six-well plate inserts as described in ref. 3 with some modifications. Briefly, PCNs were isolated from E15.5 embryos and plated on the cell-culture inserts with a 3-μm pore size (08-771-3; Fisher Scientific). Neurites were separated from cells on DIV10 for further analysis. To transfect PCNs, we performed magneto-fection using NeuroMag (OZ Biosciences) according to the manufacturer's protocol at the DIV specified in the text and subjected to live-cell imaging. Transfection with mtGFP was done following the manufacturer's recommendations. Our PCN transfection rate was 1 to 5%. PCNs were chosen for imaging analysis using the following criteria: GFP signal above background threshold with TMRM accumulation in at least some of the mitochondria with processes that can be followed and measured. GFP- and TMRM-positive PCNs that were entangled with other GFP/TMRM-positive PCNs were excluded to avoid incorrectly assigning distances. Using these criteria, 5 to 10 PCNs were imaged and analyzed per embryo, and PCNs were analyzed from three individual embryos per experiment. The exact number of PCNs analyzed per experiment is given in each figure legend.

Mitochondrial Isolation. Brain mitochondria were isolated by Percoll density centrifugation as described in ref. 45 and modified in ref. 9. Neuronal mitochondria were isolated from PCNs and neurites using anti-TOM22 antibodies immobilized on magnetic beads provided with the MACS Isolation Kit (Miltenyi Biotec). Briefly, mouse primary cortical neurons from E15.5 Swiss Webster mice were plated on six-well cell-culture plate inserts coated with poly-L-lysine and cultured in plating medium (MEM), 10% FBS,

NEUROSCIENCE

www.manaraa.com

0.45% glucose, 1 mM sodium pyruvate, 2 mM glutamine, 20 U/mL penicillin, and 20 μg/mL streptomycin for 3 h and then maintained in serum-free Neurobasal medium containing B27 supplement (Life Technologies), 0.5 mM glutamine, and 25 μM glutamate for the first 3 d. At day 10 in vitro, neurons and neurites were separated by scraping them off the top (PCNs) or bottom (neurites) surfaces of the inserts. Then, both PCNs and neurites were homogenized by passing them through a 27-gauge needle 20 times. The homogenate was spun down at $10,000 \times g$ for 10 min and cytosolic fractions were collected for cyt c immunoblotting. The pellets were resuspended in the separation buffer and incubated for 1 h with TOM22-conjugated magnetic beads followed by separation of mitochondria on the MACS separation columns. Collected mitochondria were either tested for $\Delta\psi_m$ immediately or frozen at −80 °C for immunoblotting.

Fluorescence Microscopy. For fluorescence imaging, we used an IX-81-DSU Olympus microscope, equipped with an H117 motorized linear-encoded xy stage (Prior Scientific), Orca-R^2 CCD camera (Hamamatsu Photonics), and a Lumen 200 light source (Prior Scientific). Confocal images were taken at a magnification of 40× (UPLSAPO 40×, N.A. 0.95; Olympus) or 100× (UPLSAPO 100×O, N.A. 1.4; Olympus) with MetaMorph (Media Cybernetics) data acquisition and analysis software. The microscope was equipped with a temperature- and gas composition-controlled on-stage incubation chamber (WSKM-FI; Prior Scientific) to perform long-term live imaging at 37 °C and 5% CO$_2$.

Live-Cell Imaging. Multiwavelength fluorescence imaging was performed using the following excitation (emission) wavelengths obtained with filters: 473/31 (520/35) nm for GFP or nonoxidized MitoTimer, 531/40 (593/40) nm for TMRM, MitoSOX, or oxidized MitoTimer, and 628/40 (692/40) nm for MitoView633. For FRET measurements, excitation/emission wavelengths were 430/480, 517/528, 430/528 for CFPs, yellow fluorescent proteins (YFPs), and CFP-YFP FRET signals, respectively. To minimize phototoxicity resulting from long-term illumination, intensity for excitation lights was set to 5 to 10% for TMRM, 5 to 15% for GFP, and 15 to 25% for MitoView633 while exposure was increased up to 750, 500, and 750 μs, respectively. On the indicated number of days after the transfection of neurons, half of the media was replaced with fresh media containing TMRM (or MitoView633) at 5 to 50 nM and imaging was started no less than 2 h after the incubation to allow TMRM or MitoView633 to equilibrate. Despite a variation in imaging parameters, a comparison between control and experimental conditions was done at identical imaging settings. Imaging of mitochondrial trafficking was done using wide-field mode with excitation intensities set to 1% for TMRM (50 nM) and 2% for GFP. Frames were recorded at the rate of one frame per 5 or 10 s with an UPLSAPO 100×O N.A. 1.4 objective.

Time-Lapse Live-Cell Imaging. Primary cerebrocortical neurons were plated at 3×10^5 cells per well of 96-well no. 1.5 coverglass-bottom plates (Cellvis) and transfected with the mtGFP viral construct. For TOM40 knockdown experiments, neurons were loaded with TMRM dye (50 nM) and the cell membrane-impermeable nuclear dye RedDot2 (Biotium) 3 d after transfection. For mtGFP import/accumulation experiments, neurons were loaded with TMRM dye (20 nM) immediately after the addition of the mtGFP viral construct. Sets of images were acquired every 1.5 h with an UPLSAPO 40× air 0.95 N.A. lens and analyzed as described earlier (9).

Two-Photon Live Imaging of Mouse Spinal Cord. Thy1-CFP-MitoS mice expressing mitochondria-targeted CFP in neurons were used for in vivo imaging of neuronal mitochondria. The mouse spinal cord surgery was conducted according to ref. 46. Briefly, mice were deeply anesthetized with a ketamine: xylazine mixture (90:9 mg/kg) and placed into a stereotaxic frame (Narishige) with a heating pad and provided free-flowing O$_2$ (0.9 L/min) through a stereotaxic gas mask. Access to the spinal cord was gained with a midline incision from the dorsal surface. A dorsal laminectomy and dural opening were performed. TMRM was incubated over the exposed spinal cord for at least 1 h and then washed three times with artificial cerebrospinal fluid (ACSF) before imaging. To stabilize the spinal cord from breathing artifacts during imaging, a custom-designed C-shaped stabilizer was mounted to the stereotaxic frame and dental-cemented to rostral and caudal intact spinal segments adjacent to the laminectomy. For in vivo imaging, a two-photon laser-scanning microscope was used. The microscope consists of a scan head (Ultima IV; Bruker) and a Ti:sapphire laser (Mai Tai DS; Spectra-Physics) providing 100-fs pulses at 80 MHz tuned at a wavelength of 920 nm for this study. Mitochondria-tagged protein fluorescence was detected using nondescanned photomultiplier tubes (Hamamatsu Photonics) in whole-field detection mode filtered with 531/40 (to detect CFP) and 617/73 (to detect TMRM) filter cubes. A water-immersion 16× objective lens (0.8 N.A.; CFI785; Nikon Instruments) was used to acquire

1,024 × 1,024 pixels (407.5 × 407.5 μm) images over ∼4.8 s using Prairie View software. Stacks were continuously acquired along depth (z stacks) every 2 μm from 180 to 202 μm below the surface of the spinal cord.

Single-Cell Analysis of Mitochondrial Functions in a Neuron. To quantify the relative difference in TMRM fluorescence associated with $\Delta\psi_m$, confocal z stacks of images of mtGFP-transfected neurons loaded with TMRM were deconvoluted and GFP signal was segmented using user-defined thresholds for pixel intensity. All images were processed using the Imaris (Bitplane) "surface" function. TMRM intensity values are defined as the mean signal intensity inside the respective GFP-derived surfaces. Use of the TMRM as $\Delta\psi_m$ indicator is justified by the fact that TMRM accumulation in mitochondria obeys a Nernstian equilibrium and can be used to quantitate both relative and absolute values at nonquenching concentration ranges in cells (47). The approximate distance (d) between mitochondria and a corresponding nucleus was calculated as $d = \sqrt{(x_i - x_0)^2 + (y_i - y_0)^2 + (z_i - z_0)^2}$, where x_i, y_i, and z_i are the relative coordinates of a mitochondrial volume and x_0, y_0, and z_0 are the relative coordinates of the nucleus center. In addition to TMRM fluorescence, mtGFP signal intensity linearly correlates with the concentration of the accumulated protein and was used to assess import of mitochondrial proteins (48). For other analyses including MitoTimer and mitochondrial ROS, we used MetaMorph (Media Cybernetics) and ImageJ (NIH). Stitching of multichannel 3D microscopic images was done in ImageJ based on ref. 49.

Immunostaining. PCNs were fixed in 4% paraformaldehyde in PBS for 10 min, permeabilized with 0.1% Triton X-100 in PBS for 15 min at room temperature, and subjected to immunofluorescence with the indicated primary and secondary antibodies. Samples were examined with the Olympus IX-81-DSU running in confocal mode.

Immunoblotting. Samples (isolated mitochondria or whole-cell lysates) were cleared by centrifugation at $20,000 \times g$, equal amounts of protein were separated on 4 to 12% gradient polyacrylamide gels (Invitrogen), and gels were transferred overnight onto 0.45-μm polyvinylidene difluoride (PVDF) membranes. The membranes were then incubated with the indicated primary antibodies overnight at 4 °C followed by incubation with secondary antibodies (Li-Cor) for 1 h at room temperature, which were detected using the Odyssey CLx Infrared Imaging System (Li-Cor). Band intensities were quantified using Image Studio (Li-Cor). Anti–β-actin (SC-47778; Santa Cruz Biotechnology), anti-XIAP (ab21278; Abcam), anti-Parkin2 (ab15954; Abcam), anti-PINK1 (TA324354; OriGene), anti–PSD-95 (AB9708; Millipore), anti-TOM20 (11802-1-AP; Proteintech), anti-TOM20 (42406; Cell Signaling), and anti–caspase-3 (9662; Cell Signaling) were used.

Caspase Activity Assay. For forebrain and synaptosome samples, homogenates were lysed and activity of cleaved caspase-3 and -7 was assessed by using tetrapeptide substrate (DEVD) in accordance with manufacturer recommendations (30009-2; Biotium). A 50 μM final concentration of Ac-DEVD-CHO was used for the negative control samples. Each sample was transferred to a 96-well assay white plate (Costar 3610; Corning), and caspase-3–like (DEVD-ase) activity was assessed by the increase of the intensity of fluorescence ($\lambda_{ex/em}$ 490/520 nm) by cleavage of the (Ac-DEVD)$_2$-R110 substrate every 4 min for 1 h using a multiwell plate reader (Synergy H1; BioTek). The calculated rate of the DEVD-ase activity was normalized by protein amount. For the study of neurites isolated from PCNs, of which the yield of total protein is considerably less than for whole-forebrain samples, we used immunoblotting to assess caspase-3 activity. Although not as sensitive, immunoblotting requires about 10 μg to produce reliable results, whereas the fluorogenic assay requires significantly more total protein (∼300 to 500 μg per assay counting all of the necessary controls for sensitivity/specificity) that is difficult to attain from neurites.

Assessment of Cardiolipin Externalized on the Mitochondrial Surface. Mitochondria were incubated in the presence and absence of CL-specific phospholipase A$_2$ in mitochondria-isolating buffer containing CL fatty acid-free human serum albumin (25 mg/mL) for 50 min at 4 °C as previously described (38). At the end of incubation, lipids were extracted and molecular species of cardiolipin and monolysocardiolipin were separated on a normal-phase column using a Dionex UltiMate 3000 HPLC coupled online to a linear ion-trap mass spectrometer (LXQ; Thermo Fisher) as previously described (50).

Assessment of $\Delta\psi_m$ in Isolated Mitochondria. Mitochondria were incubated in buffer media containing 5 mM Hepes (pH 7.4), 125 mM KCl, 2 mM Pi, 20 μM

EDTA, and 5 mM MgCl$_2$, supplied with 5 mM glutamate/malate and 5 mM succinate (as respiratory substrate) with 250 nM TMRM for 15 min. Then, mitochondria were spun down at 10,000 × g for 5 min and Δψ$_m$ was assessed as a ratio of TMRM accumulated in mitochondria to total TMRM remaining in the supernatant, as described in ref. 27.

Mitochondrial in Vitro Protein Import Assay. The assay was performed as previously described (9). Ornithine transcarbamylase precursor cDNA in pGEM-3Zf(+)-pOTC plasmid was transcribed and translated in vitro using the TNT Coupled Reticulocyte Lysate System (Promega) in the presence of [^{35}S] methionine (PerkinElmer). Following translation, [^{35}S]methionine-labeled pOTC was incubated with isolated mitochondria at 25 °C for the indicated times, and mitochondria containing imported OTC were collected by centrifugation (9,000 × g, 10 min) and subjected to SDS/PAGE. Mature OTC, which represents the cleaved protein after translocation into the mitochondrial matrix, was quantified by ImageJ (NIH). The data are presented as normalized by input (total [^{35}S]pOTC per lane).

Statistics. Statistical analyses were performed with OriginPro (OriginLab) software. Data were obtained from at least three independent experiments and expressed as mean ± SEM unless otherwise specified. The Student's t test for parametric data and the Mann–Whitney U test for nonparametric data were used for analysis of two groups. Paired t tests were used for experiments with multiple samples from the same source. Equal variance for parametric data was formally tested using the F test. For time-lapse image analysis of TOM40 knockdown neurons, Kaplan–Meier curves were used to estimate survival, and statistical comparisons between TOM40 knockdown and control neurons were made using the log-rank test. P values less than 0.05 were considered statistically significant.

1. Luo L, O'Leary DD (2005) Axon retraction and degeneration in development and disease. *Annu Rev Neurosci* 28:127–156.
2. Nikolaev A, McLaughlin T, O'Leary DD, Tessier-Lavigne M (2009) APP binds DR6 to trigger axon pruning and neuron death via distinct caspases. *Nature* 457:981–989.
3. Unsain N, Higgins JM, Parker KN, Johnstone AD, Barker PA (2013) XIAP regulates caspase activity in degenerating axons. *Cell Rep* 4:751–763.
4. Stevens B, et al. (2007) The classical complement cascade mediates CNS synapse elimination. *Cell* 131:1164–1178.
5. Deveraux QL, et al. (1999) Cleavage of human inhibitor of apoptosis protein XIAP results in fragments with distinct specificities for caspases. *EMBO J* 18:5242–5251.
6. Friedlander RM (2003) Apoptosis and caspases in neurodegenerative diseases. *N Engl J Med* 348:1365–1375.
7. Hartmann A, et al. (2000) Caspase-3: A vulnerability factor and final effector in apoptotic death of dopaminergic neurons in Parkinson's disease. *Proc Natl Acad Sci USA* 97:2875–2880.
8. D'Amelio M, et al. (2011) Caspase-3 triggers early synaptic dysfunction in a mouse model of Alzheimer's disease. *Nat Neurosci* 14:69–76.
9. Yano H, et al. (2014) Inhibition of mitochondrial protein import by mutant huntingtin. *Nat Neurosci* 17:822–831.
10. Lee SH, et al. (2012) Impaired short-term plasticity in mossy fiber synapses caused by mitochondrial dysfunction of dentate granule cells is the earliest synaptic deficit in a mouse model of Alzheimer's disease. *J Neurosci* 32:5953–5963.
11. Ferrer I, et al. (2012) Neurochemistry and the non-motor aspects of PD. *Neurobiol Dis* 46:508–526.
12. Reddy PH, Shirendeb UP (2012) Mutant huntingtin, abnormal mitochondrial dynamics, defective axonal transport of mitochondria, and selective synaptic degeneration in Huntington's disease. *Biochim Biophys Acta* 1822:101–110.
13. Sims NR, Anderson MF (2008) Isolation of mitochondria from rat brain using Percoll density gradient centrifugation. *Nat Protoc* 3:1228–1239.
14. Liu X, Kim CN, Yang J, Jemmerson R, Wang X (1996) Induction of apoptotic program in cell-free extracts: Requirement for dATP and cytochrome c. *Cell* 86:147–157.
15. Bulteau A-L, Szweda LI, Friguet B (2006) Mitochondrial protein oxidation and degradation in response to oxidative stress and aging. *Exp Gerontol* 41:653–657.
16. Jenner P (2003) Oxidative stress in Parkinson's disease. *Ann Neurol* 53(Suppl 3): S26–S36; discussion S36–S38.
17. Federico A, et al. (2012) Mitochondria, oxidative stress and neurodegeneration. *J Neurol Sci* 322:254–262.
18. Lin MT, Beal MF (2006) Mitochondrial dysfunction and oxidative stress in neurodegenerative diseases. *Nature* 443:787–795.
19. Laker RC, et al. (2014) A novel MitoTimer reporter gene for mitochondrial content, structure, stress, and damage in vivo. *J Biol Chem* 289:12005–12015.
20. Balaban RS, Nemoto S, Finkel T (2005) Mitochondria, oxidants, and aging. *Cell* 120: 483–495.
21. Manczak M, et al. (2006) Mitochondria are a direct site of A beta accumulation in Alzheimer's disease neurons: Implications for free radical generation and oxidative damage in disease progression. *Hum Mol Genet* 15:1437–1449.
22. Lee SK, Hollenbeck PJ (2003) Organization and translation of mRNA in sympathetic axons. *J Cell Sci* 116:4467–4478.
23. Taylor AM, et al. (2009) Axonal mRNA in uninjured and regenerating cortical mammalian axons. *J Neurosci* 29:4697–4707.
24. Jung H, Yoon BC, Holt CE (2012) Axonal mRNA localization and local protein synthesis in nervous system assembly, maintenance and repair. *Nat Rev Neurosci* 13:308–324.
25. Buckman JF, et al. (2001) MitoTracker labeling in primary neuronal and astrocytic cultures: Influence of mitochondrial membrane potential and oxidants. *J Neurosci Methods* 104:165–176.
26. Misgeld T, Kerschensteiner M, Bareyre FM, Burgess RW, Lichtman JW (2007) Imaging axonal transport of mitochondria in vivo. *Nat Methods* 4:559–561.
27. Scaduto RC, Jr, Grotyohann LW (1999) Measurement of mitochondrial membrane potential using fluorescent rhodamine derivatives. *Biophys J* 76:469–477.
28. Miller KE, Sheetz MP (2004) Axonal mitochondrial transport and potential are correlated. *J Cell Sci* 117:2791–2804.
29. Chang DTW, Rintoul GL, Pandipati S, Reynolds IJ (2006) Mutant huntingtin aggregates impair mitochondrial movement and trafficking in cortical neurons. *Neurobiol Dis* 22:388–400.
30. Dabir DV, et al. (2013) A small molecule inhibitor of redox-regulated protein translocation into mitochondria. *Dev Cell* 25:81–92.
31. Medler K, Gleason EL (2002) Mitochondrial Ca(2+) buffering regulates synaptic transmission between retinal amacrine cells. *J Neurophysiol* 87:1426–1439.
32. David G, Barrett EF (2003) Mitochondrial Ca^{2+} uptake prevents desynchronization of quantal release and minimizes depletion during repetitive stimulation of mouse motor nerve terminals. *J Physiol* 548:425–438.
33. Kang JS, et al. (2008) Docking of axonal mitochondria by syntaphilin controls their mobility and affects short-term facilitation. *Cell* 132:137–148.
34. Rizzuto R, De Stefani D, Raffaello A, Mammucari C (2012) Mitochondria as sensors and regulators of calcium signalling. *Nat Rev Mol Cell Biol* 13:566–578.
35. Mangiarini L, et al. (1996) Exon 1 of the HD gene with an expanded CAG repeat is sufficient to cause a progressive neurological phenotype in transgenic mice. *Cell* 87: 493–506.
36. Ona VO, et al. (1999) Inhibition of caspase-1 slows disease progression in a mouse model of Huntington's disease. *Nature* 399:263–267.
37. Zhang Y, et al. (2006) Huntingtin inhibits caspase-3 activation. *EMBO J* 25:5896–5906.
38. Chu CT, et al. (2013) Cardiolipin externalization to the outer mitochondrial membrane acts as an elimination signal for mitophagy in neuronal cells. *Nat Cell Biol* 15: 1197–1205.
39. Sheng Z-H, Cai Q (2012) Mitochondrial transport in neurons: Impact on synaptic homeostasis and neurodegeneration. *Nat Rev Neurosci* 13:77–93.
40. Ferree AW, et al. (2013) MitoTimer probe reveals the impact of autophagy, fusion, and motility on subcellular distribution of young and old mitochondrial protein and on relative mitochondrial protein age. *Autophagy* 9:1887–1896.
41. Ashrafi G, Schlehe JS, LaVoie MJ, Schwarz TL (2014) Mitophagy of damaged mitochondria occurs locally in distal neuronal axons and requires PINK1 and Parkin. *J Cell Biol* 206:655–670.
42. Zou H, Li Y, Liu X, Wang X (1999) An APAF-1.cytochrome c multimeric complex is a functional apoptosome that activates procaspase-9. *J Biol Chem* 274:11549–11556.
43. Smith GA, et al. (2014) Progressive axonal transport and synaptic protein changes correlate with behavioral and neuropathological abnormalities in the heterozygous Q175 KI mouse model of Huntington's disease. *Hum Mol Genet* 23:4510–4527.
44. National Research Council (2011) *Guide for the Care and Use of Laboratory Animals* (National Academies Press, Washington, DC), 8th Ed.
45. Kristián T, Hopkins IB, McKenna MC, Fiskum G (2006) Isolation of mitochondria with high respiratory control from primary cultures of neurons and astrocytes using nitrogen cavitation. *J Neurosci Methods* 152:136–143.
46. Davalos D, Akassoglou K (2012) In vivo imaging of the mouse spinal cord using two-photon microscopy. *J Vis Exp* (59):e2760.
47. Gerencser AA, et al. (2012) Quantitative measurement of mitochondrial membrane potential in cultured cells: Calcium-induced de- and hyperpolarization of neuronal mitochondria. *J Physiol* 590:2845–2871.
48. Yano M, et al. (1997) Visualization of mitochondrial protein import in cultured mammalian cells with green fluorescent protein and effects of overexpression of the human import receptor Tom20. *J Biol Chem* 272:8459–8465.
49. Preibisch S, Saalfeld S, Tomancak P (2009) Globally optimal stitching of tiled 3D microscopic image acquisitions. *Bioinformatics* 25:1463–1465.
50. Atkinson J, et al. (2011) A mitochondria-targeted inhibitor of cytochrome c peroxidase mitigates radiation-induced death. *Nat Commun* 2:497.
51. Dunn KW, Kamocka MM, McDonald JH (2011) A practical guide to evaluating colocalization in biological microscopy. *Am J Physiol Cell Physiol* 300:C723–C742.

NEUROSCIENCE

Baranov et al.

www.manaraa.com